Simultaneous Single-Particle Superlocalization and Rotational Tracking

3 AUTHORS:

Yan Gu
Harvard University
12 PUBLICATIONS   **162** CITATIONS

SEE PROFILE

Gufeng Wang
North Carolina State University
53 PUBLICATIONS   **1,206** CITATIONS

SEE PROFILE

Ning jian Fang
lvyou university
**68** PUBLICATIONS   **965** CITATIONS

SEE PROFILE

Simultaneous Single-Particle Superlocalization and Rotational Tracking

Yan Gu,[†] Gufeng Wang,[‡,*] and Ning Fang[†,*]

[†]Ames Laboratory, U.S. Department of Energy, and Department of Chemistry, Iowa State University, Ames, Iowa 50011, United States and [‡]Department of Chemistry, North Carolina State University, Raleigh, North Carolina 27695, United States

ABSTRACT Superlocalization of single molecules and nanoparticles has become an essential procedure to bring new insights into nanoscale structures and dynamics of biological systems. In the present study, superlocalization is combined with the newly introduced differential interference contrast (DIC) microscopy-based single-particle orientation and rotational tracking. The new technique overcomes the difficulty in localization of the antisymmetric DIC point spread function by using a dual-modality microscope configuration for simultaneous rotational tracking and localization of single gold nanorods with nanometer-scale precision. The new imaging setup has been applied to study the steric hindrance induced by relatively large cargos in the microtubule gliding assay and to track nanocargos in the crowded cellular environment. This technique has great potential in the study of biological processes where both localization and rotational information are required.
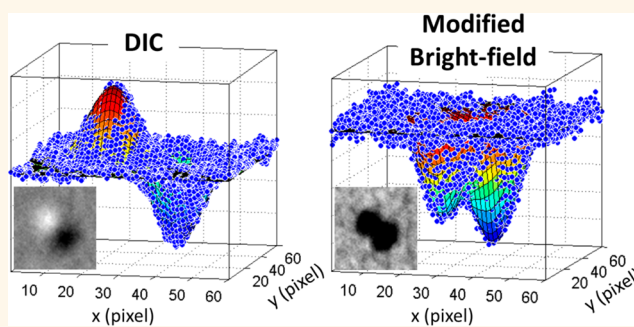
Localization of single molecules and particles in optical microscopy with a precision of 1 to 3 orders of magnitude smaller than the diffraction limit of light is often referred to as superlocalization. Nanometer-scale localization precision has been demonstrated for single fluorophores[1−8] and nonfluorescent particles.[9−11] In single-molecule or -particle tracking experiments, superlocalization has brought new insights into various biological questions, *e.g.*, the stepping mechanisms of motor proteins kinesin and myosin.[10−13] In single-molecule-based super-resolution fluorescence microscopy, such as stochastic optical reconstruction microscopy (STORM)[14,15] and photoactivated localization microscopy (PALM),[16−18] the localization precision determines the spatial resolution as individual molecules are separated spatially and temporally.

In most superlocalization analyses the centroids of single molecules/particles are found by fitting their images to the point spread function (PSF) of the optical imaging system, which is usually approximated as a 2D Gaussian function. Beyond these relatively simple cases, however, there are more complicated situations where the PSF does not resemble the Gaussian profile. For example, special care is required to minimize the localization errors when the intensity distribution of an emitting molecule is significantly affected by the emission dipole's 3D orientation.[3,4] In differential interference contrast (DIC) microscopy, the antisymmetric PSF, which is composed of apposed bright and dark parts over a gray background, cannot be fitted with a simple mathematical function; therefore, the correlation mapping algorithm has been implemented to provide nanometer-scale localization for spherical particles in 2D[10] and 3D.[9]

While tracking precise trajectories of single molecules and particles has become more attainable, a thorough understanding of a biological process frequently requires additional information such as the orientation and rotational motion of target molecules. Current techniques for acquiring orientation and rotational information of nano-objects are based on optical anisotropy of the probes. Polarized fluorescence[19,20] or dark-field scattering imaging[21] techniques convert the orientation information to image intensity, which is determined by the angle between the transition dipole of

the probe and the polarization direction of the illumination beam. Most of these methods are not directly compatible with superlocalization microscopy. For example, in defocused imaging, it is challenging to locate the center of the defocused image patterns; therefore, switching back and forth between focused and defocused imaging[22] or taking focused and defocused images simultaneously using a dual-wavelength setup[23] is necessary to obtain the accurate centroid and orientation. More recently, Ohmachi et al. developed a simultaneous 3D orientation and position tracking technique for highly fluorescent quantum rods by splitting fluorescence signals to four polarization channels.[24]

We have recently developed the single-particle orientation and rotational tracking (SPORT) technique[25,26] to visualize the motions of single rod-shaped plasmonic gold nanoparticles in DIC microscopy. The SPORT technique is especially useful in biological studies with gold nanorods as the probes because of their low cytotoxicity, large optical cross section resulting from surface plasmon resonance (SPR), and excellent photostability. However, the SPORT technique faces challenges of superlocalization similar to other rotational tracking techniques, as well as the difficulties due to the antisymmetric PSF of DIC microscopy.

In this study, we demonstrate a novel dual-modality approach for SPORT, which allows for simultaneous rotational tracking and localization of single gold nanorods with nanometer-scale precision in engineered environments and in live cells. This is realized by inserting an additional arm into the optical path of the DIC microscope for imaging in two modes simultaneously. In the additional optical arm, gold nanorod probes form modified bright-field images, allowing their positions to be determined with nanometer-scale precision. At the same time, the original DIC scheme allows for the rotational tracking of gold nanorods, thus keeping all the essential traits of the SPORT technique. Using this setup, a localization precision of less than 10 nm has been achieved for gold nanorods with an average size of 25 nm ×73 nm at a temporal resolution of 74 ms. The usefulness of the novel particle tracking strategy is demonstrated by tracking gold nanorod cargos in microtubule gliding assays and in live cells under the influence of steric hindrance.

RESULTS AND DISCUSSION

DIC/Bright-Field Dual-Modality Microscopy. The dual-modality setup is modified from a Nikon Eclipse 80i DIC microscope equipped with two Nomarski prisms (Figure 1A) for taking images in DIC and bright-field modes simultaneously. The first Nomarski prism splits the illumination white light into two beams that are mutually orthogonally polarized and laterally shifted by a small shear distance d. These two beams result in two intermediate bright-field images behind the

microscope objective and tube lens. The presence of the second Nomarski prism shifts the two intermediate images back by the same shear distance d.

In the dual-modality imaging, instead of intercepting the images behind the tube lens, the intermediate images are collimated again and divided by a 560 nm long pass dichroic mirror into two channels. Proper band-pass filters are inserted into the two light paths to select a wavelength of 700 nm for DIC imaging and 540 nm for bright-field imaging. The bandwidth of both filters is 20 nm. These two wavelengths correspond to the longitudinal and transverse SPR modes of the gold nanorods (25 nm × 73 nm), respectively.

In the 700 nm DIC channel, the second polarizer projects the two intermediate bright-field images to the same polarization plane and interference occurs, yielding typical bright/dark DIC images on a gray background (Figure 1B). This channel tracks the 3D orientation of the nanorod's longitudinal SPR mode.

In the 540 nm bright-field channel, the two mutually shifted intermediate images are projected onto the camera without interference in the absence of the second polarizer, forming an overlaid bright-field image for the gold nanorod's transverse SPR mode. A gold nanorod shows as two partially overlapped dark lobes, mutually shifted by the shear distance d, on a bright background (Figure 1C). On this microscope utilizing the de Sénarmont bias retardation, the two Nomarski prisms are fixed in the light path, and the shear direction is accurately aligned at 45° along the northwest−southeast direction. The presence of two Nomarski prisms in this modified bright-field microscopy imaging results in a new PSF that can be approximated as a double-peak Gaussian profile; therefore, the centroid of a single particle can be located by nonlinear least-squares fitting of the two dark lobes with the following double-peak Gaussian function:

$$I = I_b - A_1 \cdot e^{-\left[\frac{(x-x_0)^2}{2\sigma_{x1}^2} + \frac{(y-y_0)^2}{2\sigma_{y1}^2}\right]}$$
$$- A_2 \cdot e^{-\left[\frac{[x-(x_0-d/\sqrt{2})]^2}{2\sigma_{x2}^2} + \frac{[y-(y_0-d/\sqrt{2})]^2}{2\sigma_{y2}^2}\right]} \quad (1)$$

where I_b is the background intensity, which is determined by the exposure time and the camera gain; A_1 and A_2 are the amplitudes of the two Gaussians; d is the shear distance in the northwest−southeast direction (Figure 1C); x_0 and y_0 are the coordinates of the centroid of the first Gaussian (indicated by the white cross in Figure 1C); and σ_{x1}, σ_{y1} and σ_{x2}, σ_{y2} are the standard deviations of the x and y components, respectively, for the two Gaussian peaks (Figure 1D).

The shear distance d is an intrinsic property of the Nomarski prisms and the focusing optics and also depends on the illumination wavelength. Two pairs of Nomarski prisms with different shear distances were tested by taking images of a gold nanorod and a
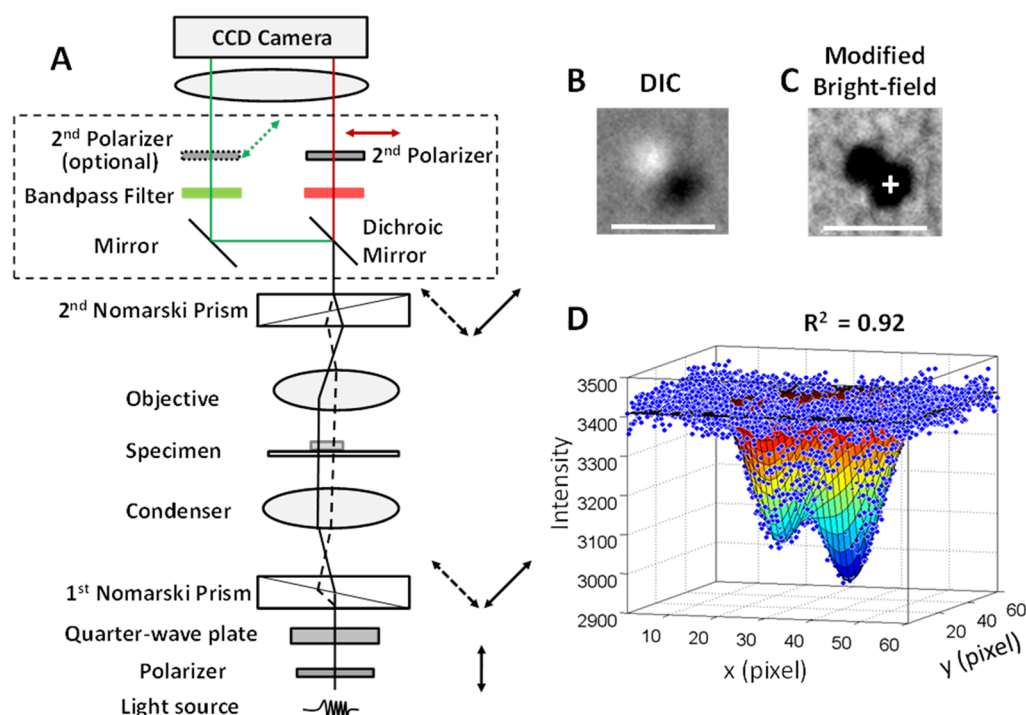
Figure 1. Dual-modality single-particle localization and rotational tracking technique. (A) Schematic diagram of the dual-modality microscope. (B) DIC image of a 200 nm polystyrene bead captured under the modified microscope. (C) Double-Gaussian bright-field image. The white cross denotes the centroid (x_0, y_0) of one of the dark lobes. These coordinates are used in eq 1. (D) Fitting of the image in (C) with a 2D inverse double-peak Gaussian function (rainbow contour). The blue dots are the measured intensities at each coordinate. The scale bars in (B) and (C) represent 1 μm.

200 nm polystyrene particle at different orientations (Figure S1). The shear distances of these Nomarski prisms were measured by fitting the modified bright-field images of the polystyrene particle with eq 1. The shear distances of these two sets of Nomarski prisms at the wavelength of 540 nm were found to be 290 ± 3 and 189 ± 3 nm, respectively. The Nomarski prisms with a larger shear distance generate more accurate results in double-peak Gaussian fitting because they separate the two peaks farther apart.

The relative intensity of the two dark lobes (the ratio of A_1 to A_2) is dependent on the orientation of the gold nanorod and the bias retardation, which is intentionally introduced as a phase shift between the two wavefronts passing through the specimen by adjusting the polarizer and quarter-wave plate settings to increase DIC image contrast.[27] Figure S2 shows an example of the DIC and modified bright-field images of the same gold nanorod at three different orientations using the pair of Nomarski prisms with the larger shear distance.

In the rest of discussion in this paper, this modified bright-field microscopy imaging mode will be referred to as the *double-Gaussian* method for superlocalization of gold nanorods.

Alternative Configuration. In the Nomarski DIC mode, the second polarizer is set at 90° with respect to the first polarizer so that final DIC images are generated with equal contributions from two orthogonally polarized light beams passing through the sample. When

the second polarizer is removed from the light path, we obtain the modified bright-field images with two dark lobes, as described in the previous section. When the second polarizer is set at 45° with respect to the first polarizer, one of the two orthogonally polarized beams is blocked, leaving only one dark spot in the final image of a gold nanorod. This alternative approach for localizing gold nanorods will be referred to as the *single-Gaussian* method.

The images of a gold nanorod and a 200 nm polystyrene particle during a 360° rotation under each of these different polarizer settings are shown in Figure S3A. With the second polarizer setting of 45°, the remaining dark spot can be nonlinear least-squares fitted with a 2D Gaussian function to locate the particle (Figure S3B, C), and the intensity changes with respect to the orientation of the nanorod's short axis, as the observation wavelength corresponds to the transverse SPR mode of the gold nanorod (Figure S4). The two 45° polarization configurations result in slightly different signal intensities once again due to the intentionally introduced bias retardation.[27] It should be pointed out that the accuracy in the measured distance is mostly independent of the nanorod's orientation; however, the localization precision varies as the nanorod's image contrast changes with its orientation.

The comparison of the double- and single-Gaussian methods is done by measuring the distances between the two particles at different orientations as shown in

Figure S3A. These two sets of measured distances are virtually identical. Therefore, the single-Gaussian method will be used exclusively in the rest of our discussions because of its mathematical simplicity.

The localization precision of the single-Gaussian method is obtained by recovering the positions of gold nanorods in a stepping experiment on a high-precision piezoelectric stage (Figure S5). The measured step sizes by localizing the particles are consistent with the designated values. The localization precision from nonlinear least-squares fitting is determined to be 2−5 nm at a temporal resolution of 74 ms, similar to those obtained for 40 nm gold nanospheres.[9]

Dual-Modality Imaging in Microtubule Gliding Assays. The microtubule gliding assays have shown great potential to serve as a transport system for shuttling and sorting nanocargos in engineered environments.[28−31] In these assays, motor proteins, such as kinesin, are precoated on a substrate and propel microtubule fragments. A microtubule can rotate along its longitudinal axis when it glides on the substrate, depending on the number of protofilaments it is composed of. We have previously demonstrated that gold nanorods with an average size of 10 nm × 35 nm attached on gliding/rotating non-13-protofilament microtubules displayed periodic bright and dark DIC image patterns, while nanorods attached on 13-protofilament microtubules displayed nearly constant DIC intensities.[26] Fluorescence interference contrast microscopy has shown that full-length kinesin motors elevate gliding microtubules by only 17 ± 2 nm over the surface.[32] Small cargos such as 20 nm quantum dots[33] or 10 nm × 35 nm gold nanorods[26] do not impede the self-rotation of microtubules; however, larger cargos such as microbeads do obstruct the self-rotation, but have a minimal effect on the forward speed of the microtubule carrier.[33]

In order to utilize molecular motors as nanoengines to transport cargos in engineered systems, it is important to understand how the transport system responds to the steric hindrance created by relatively large cargos in the gliding assay. In the current study, we carry out similar microtubule gliding experiments with larger gold nanorods with an average size of 25 nm × 73 nm. The short axis of these nanorods is the same as the outer diameter (25 nm) of the microtubules. The orientation and location of gold nanorods are obtained simultaneously at a temporal resolution of 74 ms using the single-Gaussian method.

In our experiments, the gold nanorods are surface-modified with neutravidin and the microtubules are made from a mixture of unlabeled tubulin and biotinylated tubulin at a ratio of 93 to 7. The number of biotin−neutravidin bonds between a nanorod and a microtubule is a key factor that affects the nanorod's motions during transport. When a nanorod's long axis is aligned parallel to a microtubule, the contact area of the two rod-shaped objects is maximized to allow an average of four biotin−neutravidin bonds. When a nanorod's long axis is perpendicular to a microtubule, the contact area is minimized to result in as few as one biotin−neutravidin bond. (See Supporting Information for detailed calculations.)

The parallel geometry does not create significant steric hindrance, and the nanorods in this geometry will behave similarly to that in the previous reports.[26,33] The perpendicular geometry with a single binding will likely result in a loosely bound nanorod and give rise to "blinking" (fast switching between bright and dark DIC image patterns). Such an example is given in Figure S6 (Movie 1). The current temporal resolution of 74 ms is likely too slow to fully resolve this type of fast, random rotation.

The more common and interesting case, which will be elucidated in greater detail here, is when a nanorod and a microtubule are aligned at an angle (neither perpendicular nor parallel) and held together with multiple bonds (likely 2−4 bonds under our experimental conditions). In this case, a nanorod is more strongly bound to a microtubule, and its motion is no longer determined predominately by the thermal noise, as the steric hindrance created from the nanorod/microtubule geometry and the obstacles present in the course of transport becomes an important factor. Figure 2 (Movie 2) shows an example where a gold nanorod travels nearly half a circle with a distance of ∼24 μm on a gliding microtubule. The nanorod shows a mainly bright image while traveling southwest, then a mainly dark image after turning ∼90° toward northwest, and finally a mainly bright image again after making another turn toward northeast.

The relatively stable DIC intensities on the time scale of seconds suggest that the nanorod was rather firmly attached to the microtubule through multiple biotin−neutravidin bonds. However, the recorded DIC intensity traces still show significant fluctuations, indicating that the nanorod changes its orientation intermittently from time to time due to the steric hindrance. These rotational motions are often accompanied by lateral movement of the nanorod to new positions found in the x and y trajectories.

Two interesting segments of this transport event are explained in detail as follows. In the first segment (14−22 s, Figures 2C and S7A), the microtubule glides at a nearly constant speed of 0.35 μm/s, which is evident from the constant slopes observed in both the x and y trajectories. The x trajectory is smoother than the y trajectory, which can be explained by the fact that the microtubule moves in the x direction and it is much more likely for the nanorod to swing from side to side (y) than to move back and forth (x). Interestingly, the gold nanorod changes its orientation drastically when the microtubule changes its gliding direction at 15−16 s or when the trajectory shows a sudden "jump" (a distance of ∼70 nm in the y trajectory) at ∼18.5 s. The moving directions of the gold nanorod before and after the drastic orientation changes are guided by the pink dashed lines on the y
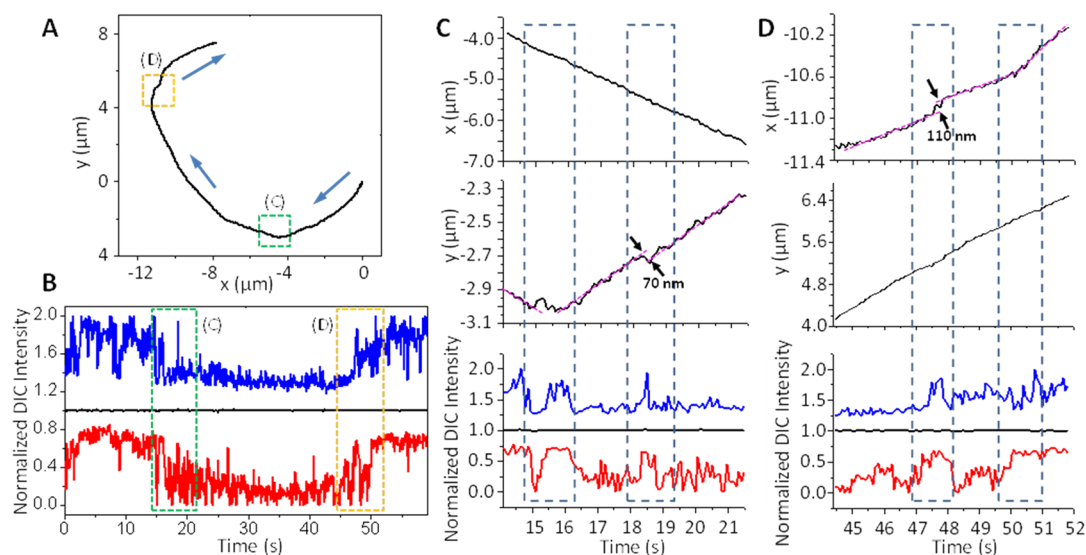
Figure 2. Motions of a gold nanorod attached to a gliding microtubule. (A) Moving trace of the gold nanorod over a time span of 59.2 s. The positions of the gold nanorod are determined by using the single-Gaussian method. (B) DIC intensity traces of the nanorod under the dual-modality microscope. The bright and dark intensities are shown in blue and red, respectively, and the average background intensities are shown in black. The green (C) and orange (D) boxes highlight two interesting segments where the transport direction is being changed and significant rotational motions are observed. (C, D) The x and y displacements and the corresponding DIC intensity traces of the gold nanorod from the two highlighted segments. The transition points with significant rotational behaviors are highlighted in the blue rectangles. The trajectories of the gold nanorod before and after the rotations are highlighted by the pink dashed lines. The calculated azimuthal and polar angles of the gold nanorods during these two segments are shown in Figure S7.

trajectory. The nanorod changes its orientation possibly because they are shunted by road blocks, such as other microtubules, aggregates of kinesin molecules, or unpolymerized tubulin monomers.[34,35] The microtubule and nanorod are caused to rotate in order to evade the steric hindrance, which results in the sudden changes in the nanorod's orientation and position. In the second segment (44−52 s, Figures 2D and S7B), the microtubule moves mainly in the y direction, which results in a rather smooth y trajectory. The rotations of the gold nanorod are accompanied by a shift of the trace at 47.5 s and a change in the moving direction at 50.0 s.

Superlocalization and Rotational Tracking of Endocytosed Gold Nanorods in a Live Cell. The cytoskeleton in a live mammalian cell is composed of interweaving microtubules and actin filaments.[36,37] Cargos are transported by molecular motors including kinesin, dynein, and myosin along the microtubule and actin filament tracks.[34] How the cargos are transported in the complex cytoskeleton system and in a crowded environment is intriguing because it is closely related with the cooperation and cross-talk among the motor proteins and the intracellular transport mechanism, but requires further study. The transport of cargo in a complex cytoskeleton environment has been studied using bright-field microscopy with pigment granules as the cargo[38] and fluorescent microscopy with fluorescently labeled organelles.[39] The directed transport of cargos is affected in regions where space is limited by the crowded cytoskeleton such as the cortex of the cell.[39,40] We previously used the SPORT technique to demonstrate that
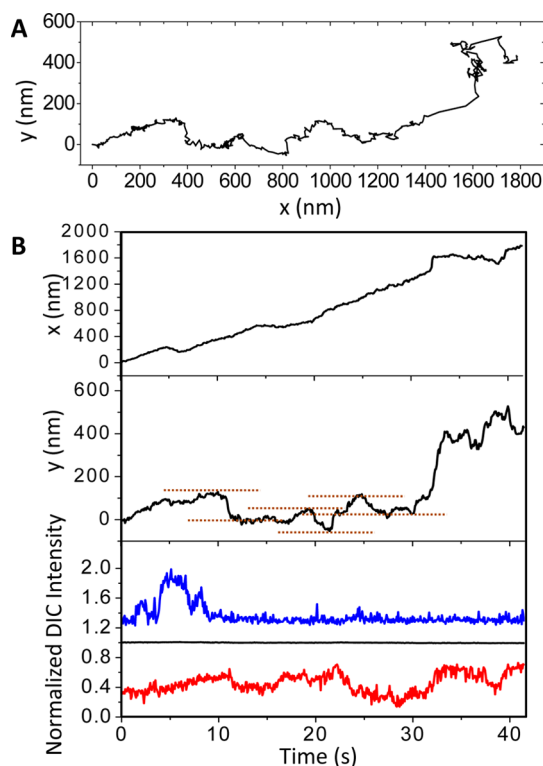
Figure 3. Lateral displacement and DIC intensities of a gold nanorod transported in a live cell. (A) Moving trace of the gold nanorod. (B) The x and y displacements and the DIC intensity traces. The lateral shifts are guided by the horizontal dashed lines. The nanorod's coordinate is set to (0, 0) at time 0.

nanocargos tend to keep their orientation during directed transport along microtubule tracks.[26,41] In this study, we

visualized the fluctuation of the cargo's orientation caused by the steric hindrance of the surrounding environment.

We imaged the transport of endocytosed transferrin-modified gold nanorods in live PC12 cells using the new imaging setup. The DIC images of the nanorods show that the rotation of the gold nanorods was common when they are transported in the cortical area where the cytoskeleton is rather crowded. One example is shown in Figure 3 (Movie 3). The gold nanorod in this example was transported over a distance of ~2 μm in the x direction. The nanorod wiggled from side to side of the microtubule track during transport, reflected by the 80−170 nm lateral displacements in the y direction, e.g., at 11, 20, and 36 s (Figure 3B). The lateral displacements are comparable to the diameter of early endosomes. It is interesting to note that at the moments of the wiggling motion the DIC intensities also indicate a wiggling motion by displaying noncorrelated bright/dark intensity changes (Figure S8). The correlation of DIC intensity with the lateral displacement and the slow rotation pattern show that the rotation of the nanorod is not caused by rotational diffusion of the vesicle.[42]

The correlated wiggling motion and the orientation changes of the gold nanorod indicate that the transport of the cargo is far from a smooth process. An important factor could be the steric hindrance caused by the crowded environment since there are interweaving actin filaments and microtubules around the cortical area of the cells. The cargo has to evade the obstruction from the interweaving microtubules and actin filaments in order to move forward. Note that the overall transport velocity is around 0.05 μm/s, much smaller than the directed transport rate on microtubule tracks[43] and actin filaments,[11,12] which also provides the evidence that the transport is hindered.

CONCLUSIONS

In summary, a novel dual-modality imaging technique has been developed to superlocalize a single gold nanorod while providing its orientation and rotational information. The superlocalization of the gold nanorod was achieved by curve fitting the modified bright-field images generated by one of the two beams laterally shifted by the Nomarski prism in a DIC microscope. The orientation and rotational information is derived from the DIC images of the gold nanorods. This new single-particle tracking technique is a significant improvement over existing nonfluorescent particle tracking techniques. Due to the advantages of this technique, it can be applied in the study of many biological processes that require both precise localization and the orientation and rotational information of the nanoprobes.

It should be noted that the temporal resolution is currently limited by the achievable signal-to-noise ratio (SNR) in the modified bright-field channel. Unlike the dark background on fluorescence images, the high background on bright-field images leads to greatly reduced SNR; therefore, the temporal resolution of 74 ms is required to achieve the reported nanometer-scale localization precision with a 100 W halogen lamp. By switching to a more intense laser light source or allowing lower localization precision, a higher temporal resolution can be achieved.

The usefulness of this technique has been demonstrated by dynamic tracking of single gold nanorod cargos in microtubule gliding assays and in live cells. The new imaging technique makes it possible in future studies to acquire critical knowledge in order to realize the transport of larger and heavier cargos in micro transport systems using molecular motors. On the other hand, the hustle of the cargo by the obstacles is an important observation associated with intracellular transport where steric hindrance exists in the crowded cellular environment. Further studies will lead to our understanding of how competing kinesin and dynein motors work together to overcome constant obstacles in intracellular transport.

METHODS

Sample Preparation. The cetyltrimethylammonium bromide (CTAB)-capped 25 nm × 73 nm gold nanorods (Nanopartz, Loveland, CO, USA) were washed and resuspended in 18.2 Ω Milli-Q water before surface modification. To change the surface charge from positive to negative, the gold nanorods were modified with transferrin through a polyethylene glycol (PEG)-thiol linker. The detailed procedures of nanorod surface modifications and polystyrene beads sample preparations can be found in the Supporting Information.

Precision and Accuracy Measurement on the Piezo-Stage. A 3D piezoelectric stage was installed on an inverted Zeiss Axiovert 100 TV microscope. The microscope was equipped with two Nomarski prisms, two polarizers, a condenser, and a 100× oil immersion objective. Gold nanorods dispersed in Milli-Q water were immobilized on a clean coverslip, and the sample slide was stepped in either the x or y direction by the piezoelectric stage with sub-nanometer precision. The DIC images were captured at 700 nm, and the bright-field images were captured at 540 nm. Three particles at different orientations were captured, which

show completely dark, completely bright, and half dark/half bright DIC images, respectively. The averaged signal-to-noise ratio of the bright-field images of the three nanorods is better than 10. The step size for each movement was 40 nm. At each position, 50 frames of images were taken at a temporal resolution of 74 ms. The coordinates of each gold nanorod in each frame were determined using the single-peak 2D Gaussian fitting of the bright-field images, and 50 x or y coordinates were plotted as one step. The precision of the single-particle tracking was calculated as the standard deviation of the x or y coordinates in each step, and the accuracy of the step measurements was determined as the standard deviation of the step sizes calculated as the difference between the averaged x or y coordinates for each two steps.

Microtubule Gliding Assays. The protocol was modified from the procedures reported in our previous publication.[25] Detailed procedures of the extraction of full-length kinesin, surface modification of gold nanorods with neutravidin, and preparation of biotinylated 12-protofilament microtubules can be found in the Supporting Information. A chamber was formed by placing a clean glass coverslip on top of a clean glass slide

with two pieces of double-sided tape serving as spacers. BRB80 solution containing 0.5 mg/mL casein (Sigma, St. Louis, MO, USA) was flowed into the chamber, and the chamber was kept at room temperature for 5 min. BRB80 solution containing 0.2 mg/mL casein, 0.2 mM MgATP, and kinesin was then introduced into the chamber to replace the previous solution. After 5 min, BRB80 solution containing 0.2 mg/mL casein, 0.2 mM MgATP, 10 μM Taxol, and microtubules was introduced into the chamber and kept at room temperature for 5 min. After that, BRB80 solution containing 0.2 mg/mL casein, 0.2 mM MgATP, 10 μM Taxol, and neutravidin-modified gold nanorods was flowed into the chamber and incubated at room temperature for 7 min. Finally, the chamber was filled with BRB80 solution containing 0.2 mg/mL casein, 1 mM MgATP, and 10 μM Taxol with an oxygen-scavenging system [50 μg/mL glucose oxidase (Sigma), 4 μg/mL catalase (Sigma), 1% (w/v) glucose (Sigma), and 0.1% (v/v) mercaptoethanol (Fluka)]. Between the steps, the chamber was washed twice with BRB80 solution containing 0.2 mg/mL casein and 0.2 mM MgATP. The motions of the gold nanorods attached with the microtubules were then imaged under our dual-modality microscope.

Cell Cultures and Live Cell Imaging. PC 12 cells (CRL 1721.1, ATCC, Manassas, VA, USA) were cultured on 22 mm × 22 mm poly-L-lysine-coated coverslips in six-well cell culturing plates. Complete cell culturing medium composed of F12K cell culturing medium (ATCC), 15% horse bovine serum (ATCC), and 2.5% fetus bovine serum (ATCC) was added to the plates. After the cell culture covered 70% of a coverslip, 40 μL of transferrin-modified gold nanorod solution was added to each of the plates and incubated for 1 h. After that, the cell coverslip was placed on a clean glass slide for imaging. Two pieces of double-sided tape act as spacers between the glass slide and the coverslip to form the chamber. A 30 μL portion of F12K cell culture medium was added to the chamber to sustain the cells.

Dual-Mode Imaging and Data Analysis. Movies of gliding assays and live cell experiments were taken under the dual-mode microscope modified from an upright Nikon 80i microscope. All movies were taken at the temporal resolution of 74 ms. The images and movies were all processed in ImageJ and Matlab. The 2D Gaussian fitting and single-particle tracking (including position and orientation) were all done automatically by running the programs written in MATLAB.

Conflict of Interest: The authors declare no competing financial interest.

Supporting Information Available: Supplementary figures and movies; Additional experimental procedures. This material is available free of charge *via* the Internet at http://pubs.acs.org.

REFERENCES AND NOTES

1. Gordon, M. P.; Ha, T.; Selvin, P. R. Single-Molecule High-Resolution Imaging with Photobleaching. *Proc. Natl. Acad. Sci. U.S.A.* **2004**, *101*, 6462–6465.
2. Yildiz, A.; Selvin, P. R. Fluorescence Imaging with One Manometer Accuracy: Application to Molecular Motors. *Acc. Chem. Res.* **2005**, *38*, 574–582.
3. Enderlein, J.; Toprak, E.; Selvin, P. R. Polarization Effect on Position Accuracy of Fluorophore Localization. *Opt. Express* **2006**, *14*, 8111–8120.
4. Mortensen, K. I.; Churchman, L. S.; Spudich, J. A.; Flyvbjerg, H. Optimized Localization Analysis for Single-Molecule Tracking and Super-Resolution Microscopy. *Nat. Methods* **2010**, *7*, 377–381.
5. Churchman, L. S.; Okten, Z.; Rock, R. S.; Dawson, J. F.; Spudich, J. A. Single Molecule High-Resolution Colocalization of Cy3 and Cy5 Attached to Macromolecules Measures Intramolecular Distances through Time. *Proc. Natl. Acad. Sci. U.S.A.* **2005**, *102*, 1419–1423.
6. Toprak, E.; Balci, H.; Blehm, B. H.; Selvin, P. R. Three-Dimensional Particle Tracking *via* Bifocal Imaging. *Nano Lett.* **2007**, *7*, 2043–2045.
7. Agrawal, A.; Deo, R.; Wang, G. D.; Wang, M. D.; Nie, S. M. Nanometer-Scale Mapping and Single-Molecule Detection with Color-Coded Nanoparticle Probes. *Proc. Natl. Acad. Sci. U.S.A.* **2008**, *105*, 3298–3303.
8. Pertsinidis, A.; Zhang, Y.; Chu, S. Subnanometre Single-Molecule Localization, Registration and Distance Measurements. *Nature* **2010**, *466*, 647–651.
9. Gu, Y.; Di, X.; Sun, W.; Wang, G.; Fang, N. Three-Dimensional Super-Localization and Tracking of Single Gold Nanoparticles in Cells. *Anal. Chem.* **2012**, *84*, 4111–4117.
10. Gelles, J.; Schnapp, B. J.; Sheetz, M. P. Tracking Kinesin-Driven Movements with Nanometre-Scale Precision. *Nature* **1988**, *331*, 450–453.
11. Levi, V.; Gelfand, V. I.; Serpinskaya, A. S.; Gratton, E. Melanosomes Transported by Myosin-V in Xenopus Melanophores Perform Slow 35 nm Steps. *Biophys. J.* **2006**, *90*, L7–L9.
12. Pierobon, P.; Achouri, S.; Courty, S.; Dunn, A. R.; Spudich, J. A.; Dahan, M.; Cappello, G. Velocity, Processivity, and Individual Steps of Single Myosin V Molecules in Live Cells. *Biophys. J.* **2009**, *96*, 4268–4275.
13. Yildiz, A.; Forkey, J. N.; McKinney, S. A.; Ha, T.; Goldman, Y. E.; Selvin, P. R. Myosin V Walks Hand-over-Hand: Single Fluorophore Imaging with 1.5-nm Localization. *Science* **2003**, *300*, 2061–2065.
14. Rust, M. J.; Bates, M.; Zhuang, X. W. Sub-Diffraction-Limit Imaging by Stochastic Optical Reconstruction Microscopy (STORM). *Nat. Methods* **2006**, *3*, 793–795.
15. Huang, B.; Wang, W. Q.; Bates, M.; Zhuang, X. W. Three-Dimensional Super-Resolution Imaging by Stochastic Optical Reconstruction Microscopy. *Science* **2008**, *319*, 810–813.
16. Betzig, E.; Patterson, G. H.; Sougrat, R.; Lindwasser, O. W.; Olenych, S.; Bonifacino, J. S.; Davidson, M. W.; Lippincott-Schwartz, J.; Hess, H. F. Imaging Intracellular Fluorescent Proteins at Nanometer Resolution. *Science* **2006**, *313*, 1642–1645.
17. Manley, S.; Gillette, J. M.; Patterson, G. H.; Shroff, H.; Hess, H. F.; Betzig, E.; Lippincott-Schwartz, J. High-Density Mapping of Single-Molecule Trajectories with Photoactivated Localization Microscopy. *Nat. Methods* **2008**, *5*, 155–157.
18. Shroff, H.; Galbraith, C. G.; Galbraith, J. A.; Betzig, E. Live-Cell Photoactivated Localization Microscopy of Nanoscale Adhesion Dynamics. *Nat. Methods* **2008**, *5*, 417–423.
19. Sabido-David, C.; Brandmeier, B.; Craik, J. S.; Corrie, J. E. T.; Trentham, D. R.; Irving, M. Steady-State Fluorescence Polarization Studies of the Orientation of Myosin Regulatory Light Chains in Single Skeletal Muscle Fibers Using Pure Isomers of Iodoacetamidotetramethylrhodamine. *Biophys. J.* **1998**, *74*, 3083–3092.
20. Inoue, S.; Shimomura, O.; Goda, M.; Shribak, M.; Tran, P. T. Fluorescence Polarization of Green Fluorescence Protein. *Proc. Natl. Acad. Sci. U.S.A.* **2002**, *99*, 4272–4277.
21. Sonnichsen, C.; Alivisatos, A. P. Gold Nanorods as Novel Nonbleaching Plasmon-Based Orientation Sensors for Polarized Single-Particle Microscopy. *Nano Lett.* **2005**, *5*, 301–304.
22. Toprak, E.; Enderlein, J.; Syed, S.; McKinney, S. A.; Petschek, R. G.; Ha, T.; Goldman, Y. E.; Selvin, P. R. Defocused Orientation and Position Imaging (DOPI) of Myosin V. *Proc. Natl. Acad. Sci. U.S.A.* **2006**, *103*, 6495–6499.
23. Xiao, L.; Wei, L.; Liu, C.; He, Y.; Yeung, E. S. Unsynchronized Translational and Rotational Diffusion of Nanocargo on a Living Cell Membrane. *Angew. Chem., Int. Ed.* **2012**, *51*, 4181–4184.
24. Ohmachi, M.; Komori, Y.; Iwane, A.; Fujii, F.; Jin, T.; Yanagida, T. Fluorescence Microscopy for Simultaneous Observation of 3d Orientation and Movement and Its Application to Quantum Rod-Tagged Myosin V. *Proc. Natl. Acad. Sci. U.S.A.* **2012**, *109*, 5294–5298.
25. Gu, Y.; Sun, W.; Wang, G. F.; Fang, N. Single Particle Orientation and Rotation Tracking Discloses Distinctive Rotational Dynamics of Drug Delivery Vectors on Live Cell Membranes. *J. Am. Chem. Soc.* **2011**, *133*, 5720–5723.

26. Wang, G.; Sun, W.; Luo, Y.; Fang, N. Resolving Rotational Motions of Nano-Objects in Engineered Environments and Live Cells with Gold Nanorods and Differential Interference Contrast Microscopy. *J. Am. Chem. Soc.* **2010**, *132*, 16417–16422.

27. Stender, A. S.; Augspurger, A. E.; Wang, G.; Fang, N. Influence of Polarization Setting on Gold Nanorod Signal at Nonplasmonic Wavelengths under Differential Interference Contrast Microscopy. *Anal. Chem.* **2012**, *84*, 5210–5215.

28. Saxton, W. M.; Porter, M. E.; Cohn, S. A.; Scholey, J. M.; Raff, E. C.; McIntosh, J. R. Drosophila Kinesin - Characterization of Microtubule Motility and ATPase. *Proc. Natl. Acad. Sci. U.S.A.* **1988**, *85*, 1109–1113.

29. Berliner, E.; Mahtani, H. K.; Karki, S.; Chu, L. F.; Cronan, J. E.; Gelles, J. Microtubule Movement by a Biotinated Kinesin Bound to a Streptavidin-Coated Surface. *J. Biol. Chem.* **1994**, *269*, 8610–8615.

30. Friedman, D. S.; Vale, R. D. Single-Molecule Analysis of Kinesin Motility Reveals Regulation by the Cargo-Binding Tail Domain. *Nat. Cell Biol.* **1999**, *1*, 293–297.

31. Kaseda, K.; Higuchi, H.; Hirose, K. Alternate Fast and Slow Stepping of a Heterodimeric Kinesin Molecule. *Nat. Cell Biol.* **2003**, *5*, 1079–1082.

32. Kerssemakers, J.; Howard, J.; Hess, H.; Diez, S. The Distance That Kinesin-1 Holds Its Cargo from the Microtubule Surface Measured by Fluorescence Interference Contrast Microscopy. *Proc. Natl. Acad. Sci. U.S.A.* **2006**, *103*, 15812–15817.

33. Nitzsche, B.; Ruhnow, F.; Diez, S. Quantum-Dot-Assisted Characterization of Microtubule Rotations during Cargo Transport. *Nat. Nanotechnol.* **2008**, *3*, 552–556.

34. Ross, J. L.; Ali, M. Y.; Warshaw, D. M. Cargo Transport: Molecular Motors Navigate a Complex Cytoskeleton. *Curr. Opin. Cell Biol.* **2008**, *20*, 41–47.

35. Seitz, A.; Surrey, T. Processive Movement of Single Kinesins on Crowded Microtubules Visualized Using Quantum Dots. *EMBO J.* **2006**, *25*, 267–277.

36. Fuchs, E.; Yang, Y. M. Crossroads on Cytoskeletal Highways. *Cell* **1999**, *98*, 547–550.

37. Klymkowsky, M. W. Weaving a Tangled Web: The Interconnected Cytoskeleton. *Nat. Cell Biol.* **1999**, *1*, E121–E123.

38. Rodionov, V.; Yi, J.; Kashina, A.; Oladipo, A.; Gross, S. P. Switching between Microtubule- and Actin-Based Transport Systems in Melanophores Is Controlled by Camp Levels. *Curr. Biol.* **2003**, *13*, 1837–1847.

39. Lang, T.; Wacker, I.; Wunderlich, I.; Rohrbach, A.; Giese, G.; Soldati, T.; Almers, W. Role of Actin Cortex in the Subplasmalemmal Transport of Secretory Granules in PC-12 Cells. *Biophys. J.* **2000**, *78*, 2863–2877.

40. Rudolf, R.; Salm, T.; Rustom, A.; Gerdes, H. H. Dynamics of Immature Secretory Granules: Role of Cytoskeletal Elements during Transport, Cortical Restriction, and F-Actin-Dependent Tethering. *Mol. Biol. Cell* **2001**, *12*, 1353–1365.

41. Sun, W.; Gu, Y.; Wang, G.; Fang, N. Dual-Modality Single Particle Orientation and Rotational Tracking of Intracellular Transport of Nanocargos. *Anal. Chem.* **2012**, *84*, 1134–1138.

42. Gu, Y.; Sun, W.; Wang, G.; Jeftinija, K.; Jeftinija, S.; Fang, N. Rotational Dynamics of Cargos at Pauses during Axonal Transport. *Nat. Commun.* **2012**, *3*, 1030.

43. Herold, C.; Leduc, C.; Stock, R.; Diez, S.; Schwille, P. Long-Range Transport of Giant Vesicles along Microtubule Networks. *ChemPhysChem* **2011**, *13*, 1001–1006.